

Anisotropy of Magnetohydrodynamic Turbulence and Polarization of the Spectral Lines of Molecules

D. S. Wiebe¹ and W. D. Watson

Physics Department, University of Illinois at Urbana-Champaign, IL 61801

ABSTRACT

The anisotropy of velocities in MHD turbulence is demonstrated explicitly by calculating the velocity gradients as a function of direction in representative simulations of decaying turbulence. It follows that the optical depths of spectral lines are anisotropic when there is MHD turbulence, and that this anisotropy influences the polarization characteristics of the emergent radiation. We calculate the linear polarization that results for the microwave lines of the CO molecule in star-forming gas and show that it is comparable to the polarization that is observed. This and our earlier result—that the anisotropy of MHD turbulence may be the cause for the absence of the Zeeman π -components in the spectra of OH mainline masers—are the first demonstrations of the occurrence of anisotropy in the optical depths caused by MHD turbulence. A non-local approximation is developed for the radiative transfer and the results are compared with those from a local (LVG) approximation.

Subject headings: ISM: magnetic fields — ISM: molecules — radio lines: ISM — polarization — turbulence

1. Introduction

Magnetic fields are believed to play a key role in the dynamics of the gas of the Galaxy, including the formation of stars and related phenomena. Dispersions in the molecular velocities are observed that exceed the thermal dispersion, and are suggestive of turbulence. Since the gas in astronomical environments tends to have high electrical conductivity, the turbulence is expected to be “MHD turbulence”—with correlated irregularities between the velocity fields, the magnetic fields, and the matter distributions. Inferences about the

¹Permanent address: Institute of Astronomy of the RAS, 48, Pyatnitskaya str., Moscow, 119017 Russia

structure of the magnetic fields in the interstellar medium are based mostly on polarimetric observations of the attenuation of starlight by dust and of the thermal emission by dust, and tend to reflect the results of averaging over dimensions larger than those at which MHD turbulence may be evident.

Goldreich & Kylafis (1981) recognized that, if anisotropies in the optical depths do occur for the spectral lines of molecules in the interstellar gas, they could cause a fractional linear polarization of a few percent in the observed spectral line radiation. More importantly, the direction of the polarization would indicate the projected direction of the magnetic field, and would serve to map the directions of the magnetic field lines. Goldreich & Kylafis (1981) perform calculations for anisotropic optical depths due to assumed anisotropies in the molecular velocities. No specific cause for the anisotropic velocities is given by Goldreich & Kylafis (1981). Anisotropic optical depths could clearly have various origins—including, simply the proximity of the edge of the gas cloud. The anisotropy due to a strong source of continuum radiation external to the gas cloud could also have a similar effect in causing linear polarization of the spectral line radiation emitted by the gas. The first effort to detect this polarization was unsuccessful. Wannier et al. (1983) attempted to measure the linear polarization of thermal lines of CO, CS, and HCN in 14 sources. Although, their upper limits were above the maximum likely polarization calculated for the CO lines, these upper limits were below (by factors of a few) the maximum likely polarizations calculated for the CS and HCN lines. Wannier et al. (1983) attributed the lack of observed polarization to the unresolved structure of the magnetic and/or velocity field. However, Barvainis & Wootten (1987) subsequently searched for polarization in an NH₃ line at higher resolution using the VLA—also without success. Further, no polarization was detected for HCO⁺ lines by Lis et al. (1988) in four dark clouds, with an upper limit of 2%. Glenn et al. (1997a) attempted to measure the polarization of HCO⁺ lines in DR 21, but also obtained only an upper limit (0.4%). Again, the absence of detectable polarization was attributed to likely unresolved structure of the magnetic/velocity fields on scales smaller than the telescope beamsize.

Stimulated by these non-detections, Deguchi & Watson (1984) performed multilevel calculations that included states of higher angular momentum and demonstrated that the polarization of a (1–0) transition is reduced by about a factor of two. This and other considerations discussed by Lis et al. (1988) reduce the expected polarization of the thermal lines to near the upper limits of 1–2% from the non-detections cited above.

The linear polarization of thermal lines was finally detected by Glenn et al. (1997b). Polarization of a spectral line of molecular CS was detected at a level of a few percent toward two evolved stars. Glenn et al. (1997b) argued that this success was a result of improved detector sensitivity and by the relatively smooth structure of the gas in the vicinity of the

evolved star—in contrast to the clumpiness of gas in star forming regions. Linear polarization of thermal spectral lines from the interstellar gas was subsequently detected by Greaves et al. (1999). The CO (2–1) and (3–2) transitions in three different locations were found to have polarizations ranging from 0.5% to 2.4%. The detection toward the DR 21 star forming region was tentative, but was later confirmed by Lai et al. (2003) for DR 21(OH). At this time, polarization of thermal CO lines has also been detected (or confirmed) in the star forming regions NGC 1333 (Girart et al. 1999), NGC 2024 (Greaves et al. 2001), the Galactic center (Greaves et al. 2002), and the Orion KL region (Girart et al. 2004). Cortes et al. (2005) report the striking observation that the polarizations of the CO (2-1) and (1-0) transitions tend to be orthogonal in DR 21(OH), with the polarization of the (1-0) being parallel to the polarization of the emission by the dust grains.

The polarization of the spectral lines of molecules may be useful as a diagnostic, not only for the magnetic fields themselves, but also for the MHD nature of the gas. One of the prominent features of MHD turbulence is its strong anisotropy (Goldreich & Sridhar 1995), which will enhance the magnitude of the optical depths of spectral lines parallel to the magnetic field in comparison with the optical depths perpendicular to the magnetic field (Watson et al. 2004). In Watson et al. (2004) we considered OH maser radiation that is created in the presence of mildly supersonic MHD turbulence. We showed that this anisotropy in the maser optical depths resulting from the anisotropy of MHD turbulent velocities can suppress the Zeeman π -components of mainline OH masers as observed—a longstanding puzzle, dating back to the first detections of masers in astronomy.

Maser radiation probes (at least directly) only the tiny fraction of the entire volume of a region in which maser spots are observed. In contrast, thermal spectral lines of molecules tend to be observed over most of the volume of molecular gas clouds. There is less doubt than for masers that the information obtained from these spectral lines is representative of a significant component of the gas. On the other hand, the effects of anisotropic optical depths are much more easily recognized for the OH mainline masers because the Zeeman π - and σ -components of these spectral lines are well separated in frequency from one another and can ordinarily be identified as σ 's or (if they were present) π 's. For spectral lines of other interstellar molecules, the Zeeman splitting is much less than the spectral linebreadth. The Zeeman components then overlap nearly completely and are essentially indistinguishable from one another. Nevertheless, an anisotropy in the optical depths is the origin of the Goldreich-Kylafis effect and, though its effect is small, can be detected. The goal of this Paper is to assess whether the anisotropy of plausible MHD turbulence is sufficient to cause the observed linear polarization of the spectral lines of CO from interstellar gas clouds that is observed. In our calculation for the OH masers, it was only necessary to integrate through a gas in which the molecular populations are independently specified in order to obtain the

intensities of the maser rays. Calculating the polarization of the thermal lines of CO is more challenging. The populations of the magnetic substates must first be found by solving rate equations with the anisotropic fluxes derived from the anisotropic optical depths.

In § 2, we calculate the velocity gradients within representative examples of turbulent MHD gas that are obtained from numerical simulations of decaying turbulence and demonstrate the anisotropy as a function of the relevant parameter here—the ratio of the Alfvén velocity to the sound speed of the gas. The existing calculational methods for the Goldreich-Kylafis effect must be augmented somewhat because of the variation in the properties of the gas from point to point, which we wish to consider. We describe how the calculations are performed in § 3. Calculations are performed, not only for the average polarization, but also to indicate how the polarization can change in direction and magnitude across the face of a gas cloud and across the profile of the spectral line. The results of these calculations are presented in § 4. A summarizing discussion is provided in § 5 where we relate the results here to our previous calculations for the polarization of continuum emission from dust grains aligned by irregular magnetic fields.

2. The Anisotropy of Velocities in an MHD Gas

Our quantitative analysis of the anisotropy is based on a numerical model of decaying MHD turbulence. We use the same results of simulations as were used in Watson et al. (2004). Only a brief description of these simulations is provided here, and we refer the reader to the earlier paper and to references therein for details. Velocity fields and magnetic fields were obtained there by integrating the equations of compressible, ideal MHD turbulence in a cubic, periodic domain on a uniform grid with 128^3 cells. The key parameter that characterizes these simulations is the ratio of the Alfvén velocity to the speed of sound v_A/c_s . This Alfvén velocity is calculated from the average magnetic field in the MHD cube—which remains constant during the time evolution of the simulation. Three values of v_A/c_s are considered—1, 3 and 10. As is standard for such simulations, the computations begin with plausible, initial velocity perturbations and evolve with time. To verify that our conclusions do not depend upon a particular statistical choice for these initial perturbations, computations were performed for three independent choices for these initial velocity perturbations for each of the values of v_A/c_s . In these simulations, the turbulent velocities evolve from supersonic (Mach number $M \simeq 4$) to subsonic ($M \simeq 0.3$). For each combination of initial perturbations and value for v_A/c_s , we have analyzed the fields at nine time steps separated in time by intervals of $0.2L_0/c_s$ —where L_0 is the physical length to be associated with the 128 grid points along the edge of the computational cube.

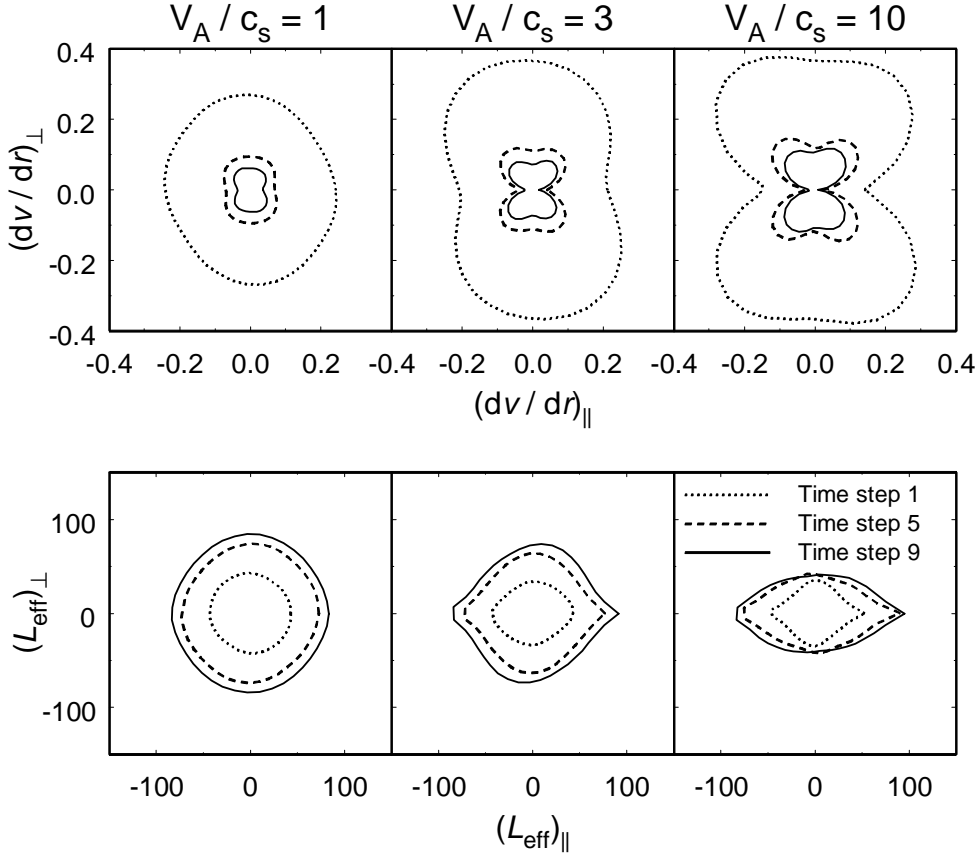


Fig. 1.— Top panel—the angular distribution of velocity gradients for three v_A/c_s values at three time steps. The distance from the coordinate origin to the curve is equal to the cube-averaged velocity gradient in the corresponding direction. Velocity is measured in units of the thermal velocity of the gas v_{th} , and the length is measured in units of the number of grid cells. Bottom panel—the angular distribution of effective interaction lengths (see text) that incorporate non-local radiative interactions between the populations of the gas molecules. The length is measured in units of the number of grid cells. The subscripts \parallel or \perp indicate directions parallel or perpendicular to the average magnetic field.

Anisotropy in the optical depths of spectral lines in an MHD gas has already been demonstrated in Watson et al. (2004). Here we delineate the anisotropy of the medium more explicitly and in more detail. There are different, approximate ways to characterize this anisotropy. We might assume that, in a supersonically turbulent medium, only the nearby region influences the populations at a given location so that the large velocity gradient (LVG) approximation is appropriate. At each of the grid points of the MHD cubes, the anisotropy can then be visualized in terms of the angular distribution of the radial (relative to the location of the particular grid point) gradients of the radial component of the turbulent velocity

$$dv_r/dr. \tag{1}$$

To examine the anisotropy in this approximation, we compute these gradients (using linear interpolations of velocities at neighboring locations) at a large number of grid points and in a large number of directions at each grid point. To simplify the computations, we only consider directions at each grid point that lie within a single plane. A plane is specified as containing the direction of the average magnetic field and the particular grid point. The planes associated with the various grid points are all parallel. The results for all grid points are then combined to obtain averaged gradients that are a function of the angle of inclination relative to the direction of the average magnetic field in the cube. These gradients are presented in Figure 1 (top panel) for the three representative time steps and for the three values of v_A/c_s that we consider. The gradients in Figure 1 are based on only a single sequence of time steps (resulting from one of the three ensembles of initial perturbations) for each of the values of v_A/c_s . For the same v_A/c_s and the same time step, the averaged gradients for the other MHD cubes differ negligibly from those that are presented.

In a statistical sense, the properties of such MHD cubes should be symmetric about the direction of the average magnetic field. The curves in Figure 1 deviate slightly from this exact symmetry because they are based on only a single MHD cube, and hence, on only a single ensemble of initial perturbations.

The direction of the average magnetic field is parallel to the horizontal axis in Figure 1. As expected, the velocity gradients are smallest in directions parallel to the magnetic field and largest in directions that are at large angles to the magnetic field. The angular variations of the gradients in Figure 1 can be seen to be similar at all times in the simulation for a specific value of v_A/c_s . In decaying turbulence, the turbulent velocities decrease with time, and hence the magnitudes of these gradients also decrease. Anisotropy is clearly evident in Figure 1 for $v_A/c_s = 3$ and 10, though not for $v_A/c_s = 1$. Note that the magnitudes of the velocity gradients in Figure 1 are given in terms of the thermal velocity of the gas $v_{\text{th}} (= \sqrt{2kT/m})$ —the thermal velocity of the dominant atomic or molecular component of the gas. The gas is mainly H_2 in the astronomical environments where our calculations are

expected to be applied and the molecules such as CO from which the spectral line radiation of interest arises are much heavier than H₂. Hence, the numerical values of the velocity gradients in Figure 1 (top panel) should be divided, for example, by the ratio (CO mass/H₂ mass)^{1/2} = 3.74 to obtain the quantities that are relevant for the radiative transport of the spectral lines of the CO molecule in the LVG approximation (see, e.g., equation 8). Note also that the dimensionless distance scale is the separation between grid points so that the gradients in Figure 1 should be divided by ($L_0/128$) to express them in terms of ordinary units for distance.

In a turbulent medium, we may expect that some remote points (as well as the nearby points) contribute to the average intensity of radiation at a given location and thus, influence the populations at this location. In contrast, in the LVG approximation where only ‘local’ interactions are considered, the extent of the region that influences the populations at a given location is assumed to be proportional to the inverse of the velocity gradient. That is, in the LVG approximation the ‘interaction length’ is assumed to be the distance over which the velocity would change by v_{th} in a given direction if its gradient were constant along this direction. In order to characterize the non-local, radiative coupling of the molecular populations and to see whether the anisotropy is preserved in the ‘non-local’ case as well, we introduce ‘effective’ interaction lengths

$$L_{\text{eff}} = \int_0^{L_{\text{max}}} dr \exp[-14(v_c - v_r)^2], \quad (2)$$

which are computed in particular directions from the specified location. Here v_c is the component of the local turbulent velocity in the direction of the integration path, v_r is this component of the turbulent velocity at a distance r from the relevant point, and the factor 14 is the ratio of molecular masses CO/H₂. In the local case, the interaction length is defined by the velocity gradient and all locations along the length of the ray have equal weight. In the non-local case, we define a length L_{max} of a ray along which the optical depths are to be calculated. Locations along this ray have different weights as determined by the Gaussian profile function in the integrand of equation (2).

The cube-averaged, angular distributions of L_{eff} are also shown in Figure 1 (bottom panel) for the choice $L_{\text{max}} = 100$ grid spacings. Again, there is almost no anisotropy in the $v_A/c_s = 1$ case, whereas the anisotropy is evident in the plots for the $v_A/c_s = 3$ and 10 cases. Since the interaction length is similar to the inverse of the velocity gradient, it is the largest in the direction of the magnetic field. The size of the interaction region increases with time as the velocity dispersion in the cube decreases. The degree of anisotropy also increases somewhat. Despite the smooth appearance of the averaged curves, there are significant

irregularities at individual locations as we will show in § 4. Just as for the average velocity gradients, the interaction lengths in Figure 1 are not exactly symmetric about the direction of the average magnetic field because Figure 1 is based on the evolution of an individual MHD cube.

3. Methods for Calculating the Polarized Radiation

The goal here is to calculate the linear polarization of spectral line radiation that emerges from a gas cloud with irregular magnetic and velocity fields represented by the MHD fields from the simulations described above. The focus is on incorporating the variations in the fields from location to location within the gas. That is, instead of using a single, averaged angular distribution for the entire cube (such as those in Figure 1) to represent the anisotropy caused by the magnetic fields and velocities in the gas, we calculate the relevant angular distribution at each grid point using the actual magnetic fields and velocities from the simulations at the particular grid point. In addition to being more realistic, this will allow us to assess what differences in the polarization characteristics can be expected for radiation that emerges from different locations on the surface of a gas cloud. The calculations are performed for the specific case of the $J = 1 \rightarrow 0$ rotational transition of the CO molecule with the usual assumption that the results will be indicative for other transitions.

The radiative transfer equations for the Stokes parameters are integrated through the cube for specific rays of spectral line radiation that emerge from the MHD cube and represent the observed radiation. For a $J = 1 \rightarrow 0$ transition with a resonant frequency ν_0 , these can be expressed as

$$\frac{d}{ds} \begin{pmatrix} I_v \\ Q_v \\ U_v \end{pmatrix} = \left[- \begin{pmatrix} A & B & 0 \\ B & A & 0 \\ 0 & 0 & A \end{pmatrix} \begin{pmatrix} I_v \\ Q_v \\ U_v \end{pmatrix} + \begin{pmatrix} k_{\pm}S_{\pm} + k_0S_0 \\ k_{\pm}S_{\pm} - k_0S_0 \\ 0 \end{pmatrix} \right] \phi\left(\nu - \nu_0 \frac{v_s}{c}\right), \quad (3)$$

where

$$\begin{aligned} A &= (k_{\pm} + k_0)/2, \\ B &= (k_{\pm} - k_0)/2, \end{aligned} \quad (4)$$

ϕ is the normalized, Gaussian line profile caused by the Doppler shifts associated with a thermal distribution of molecular velocities, v_s is the line-of-sight component of the turbulent velocity at the location s along the ray, and the absorption coefficients and source functions $(k_{\pm}, k_0, S_{\pm}, S_0)$ are obtained from the populations of the magnetic substates. Explicit expressions for $(k_{\pm}, k_0, S_{\pm}, S_0)$ can be found e.g., in Deguchi & Watson (1984) [but see Deguchi et al. (1986) for some typographical corrections]. The populations n of the magnetic substates

at a particular location along a ray are found by solving the usual rate equations in steady state

$$0 = \frac{dn_i}{dt} = -A_E n_i + R_i(n_j - n_i) + (C_{ji}n_j - C_{ij}n_i), \quad (5)$$

where A_E is the Einstein “A-coefficient” for spontaneous emission, and i ($= \pm 1, 0$) and j ($= 0$) refer to the magnetic substates of the upper $J = 1$ and lower $J = 0$ energy levels, respectively. In writing the above equations, the quantization axis and the axis for defining the polarizations are both assumed to be along the direction of the magnetic field. This simplification is appropriate when the Zeeman splitting is much less than the inverse lifetime of the excited molecular state—a requirement that is well satisfied for CO and most molecules in the interstellar gas. While the average magnetic field is always parallel to one of the sides of the cube, the local magnetic field fluctuates around this average direction. Thus, in solving equations (3) and (5), it is necessary to transform Stokes Q_ν and U_ν by a coordinate rotation at each grid point so that they are defined relative to the direction of the local magnetic field. Note also that the circular polarization is assumed to be negligible. Circular polarization is negligible when the Zeeman splitting is much less than the spectral linebreadth and the fractional linear polarization is small.

We will find the intensities to be used in calculating the R_i by two separate methods. Both are approximate and, especially for the second method, are in the spirit of approximations introduced recently by others (Ossenkopf 2002). The populations must be computed by iteration with the above equation at a large number of grid points. To find the R_i which enter into equation (5), the intensities at each grid point must be determined in a large number of directions to perform the integration over angles. So that the calculations are manageable for us, we make the approximation that the populations that enter into the calculation of the intensities for the R_i are the same as at the specific grid point for which the R_i are being calculated. Then, Stokes U is zero for the intensities that enter into the R_i , and the R_i can be expressed as (Deguchi & Watson 1984)

$$R_0 = \frac{3A_E c^2}{2h\nu_0^3} \int \frac{d\Omega}{4\pi} \int d\nu \phi \left(\nu - \nu_0 \frac{v_s}{c} \right) \sin^2 \gamma I_\nu^{\parallel}(\Omega) \quad (6)$$

and

$$R_\pm = \frac{3A_E c^2}{4h\nu_0^3} \int \frac{d\Omega}{4\pi} \int d\nu \phi \left(\nu - \nu_0 \frac{v_s}{c} \right) [I_\nu^\perp(\Omega) + \cos^2 \gamma I_\nu^{\parallel}(\Omega)]. \quad (7)$$

Here the superscripts \parallel or \perp designate linear polarizations parallel or perpendicular to the magnetic field.

The first approximate method for finding the intensities to evaluate R_0 and R_\pm is the conventional LVG approximation. To apply the approximation it must be assumed that the turbulence creates large, macroscopic velocity variations in most parts of a cube, and

hence that remote points of the gas do not interact significantly with each other through the emission and absorption of spectral line radiation. The volume that is radiatively coupled to a specific point is defined by an interaction length. The interaction length $L(\Omega)$ in the direction specified by the solid angle Ω is defined as the inverse of the velocity gradient in this direction, with the velocity expressed in units of the thermal velocity v_{th}

$$L(\Omega) = \frac{v_{\text{th}}}{dv_r/dr}. \quad (8)$$

The specific intensities $I_\nu^\perp(\Omega)$ and $I_\nu^\parallel(\Omega)$ at each grid point are then computed in the LVG approximation using the escape probability β evaluated for the optical depths

$$\tau^q(\Omega) = k^q L(\Omega) \quad (9)$$

at each grid point, where q is either \parallel or \perp . The populations entering the expressions for k^q , are assumed to be those at the specific point for which the R_i are being calculated. The values of $L(\Omega)$ at each grid point and in each direction Ω are computed from the actual velocity field in the cube of MHD velocities (typically, 1600 directions are used at each grid point for the angular integration). Iterations are performed to obtain consistent values for the populations and for the radiative rates. Explicit expressions for the polarized intensities in the LVG approximation can be found in, e.g., Deguchi & Watson (1984).

In the second approximate method—which we designate as the non-local approximation, we take into account possible radiative coupling between distant points. We integrate the formal solution of the radiative transfer equations

$$I_\nu^q(\Omega) = \int_0^L k_l^q S_l^q \phi\left(\nu - \nu_0 \frac{v_l}{c}\right) \exp[-\tau_\nu(l)] dl + I_\nu^{\text{bg}}(\Omega) \exp[-\tau_\nu(L)]. \quad (10)$$

where the optical depth is

$$\tau_\nu^q(l) = \int_0^l dl' k_{l'}^q \phi\left(\nu - \nu_0 \frac{v_{l'}}{c}\right) \quad (11)$$

by again assuming that the relative populations along the path of the integration are the same as at the particular grid point where the R_i are being computed. These relative populations are scaled with the varying gas density in the MHD cubes before performing the integrations. Here $I_\nu^{\text{bg}}(\Omega)$ is the intensity of the background radiation that may include a contribution from an external source. The absorption coefficient and the source function k_l^q and S_l^q are evaluated at the position l along the particular ray. The length L is taken to be approximately the cube dimension L_0 regardless of the location of the specific grid point

within the MHD cube. Since the MHD simulations adopt periodic boundary conditions, we use the periodicity to extend the MHD cube when necessary so that all integrals for the I_ν^q can be computed for $L \approx L_0$. Just as in the first (the LVG) approximate method, the rate equations are then solved iteratively to find the populations n_\pm and n_0 . Note that equation (10) must be solved in detail at each point in this non-local approximation for a number of frequencies ν (typically, 31 and up to 91 in some test cases), as well as angles Ω (typically, 600 at each grid point), to perform the integrations in equations (6) and (7). Hence, the non-local method requires considerably more effort than does the LVG approximation, for which a detailed calculation at a number of frequencies is not required.

The populations at the grid points of the MHD cube obtained with either the first or the second method described above are then used in the radiative transfer equation (3), which is integrated to obtain the intensities for a number of parallel rays that pass through the MHD cube and emerge at the locations of grid points on the surface. These rays represent the emergent radiation from a gas cloud.

4. Results

Calculations for the emergent, polarized radiation are performed for all of the cubes of MHD velocities and magnetic fields that are available from the simulations—cubes at nine time steps in the evolution with the three statistically chosen sets of initial velocity perturbations for each of the three values of v_A/c_s for a total of 81 MHD cubes. In all of the results that are presented, the line of sight is perpendicular to the average magnetic field. We have verified that, as expected, no significant polarization is produced in our calculations when the line of sight is parallel to the average magnetic field (the polarization is not exactly zero because of the irregularities in the magnetic field).

Once the specific MHD cube is selected, the calculations depend on only two additional quantities—the gas density and the average column density of CO molecules through the cube N_{CO} . The latter is, specifically, $N_{\text{CO}} = n_{\text{CO}} \times L_0$ where n_{CO} is the average density of CO molecules. The coefficients C_{ij} in equation (5) reflect the influence of collisional excitations and de-excitations, and are proportional to the gas density. The gas is mainly H_2 , so we use rate coefficients for CO- H_2 collisions. The calculation actually depends on only the ratios C_{ij}/A_E . Hence, we use this ratio—which we write as C/A —instead of the gas density to specify the parameters on which the calculations depend. The value of C_{ij} for de-excitation is used to specify C/A . For reference purposes, $C/A = 0.1$ for an H_2 density of 228 cm^{-3} at a temperature of 30 K. The polarization characteristics are insensitive to the adopted gas temperature, as well as to the exact values of the rate coefficients for collisional excitation.

As mentioned above, the length L of a ray for the non-local approximation in equation (10) is taken to be equal to the cube size. We tried other values for L as well, ranging from approximately half the cube size to $2L_0$, and found that the fractional polarizations for specific rays are changed by no more than 30%. The highest fractional polarizations are produced at $L \approx L_0$.

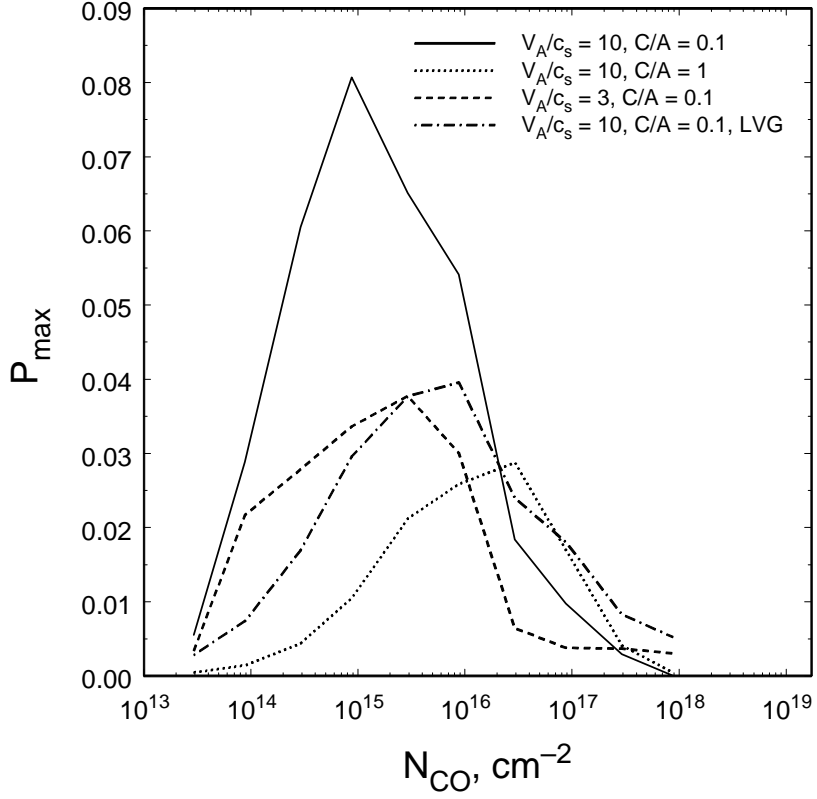


Fig. 2.— Fractional polarization P_{max} at the peak intensity of the CO spectral line as a function of the CO column density for a few choices of v_A/c_s and the gas density as indicated by C/A (5th time step). The solid, dotted, and dashed lines are obtained with the non-local approximation. The dash-dotted line is obtained with the LVG approximation.

The overall dependence of the magnitude of the fractional polarization on the CO column density is indicated in Figure 2. There, the fractional polarization at the peak intensity for the brightest ray of the $(128)^2$ rays that emerge from the grid points on the face of the cube is shown. The maximum degree of polarization occurs at a column density of $\sim 10^{15} \text{ cm}^{-2}$ which at this density and temperature corresponds roughly to $\tau \sim 1$ —the value usually assumed to be most favorable for the Godreich-Kylafis effect. Optical depth enters into the expressions for the radiative rates R_i in the rate equations, as well as in the integration of equation (3) along the line of sight for the emergent intensities. The curves in Figure 2 are reminiscent of similar diagrams for the pure LVG computations (e.g. Deguchi & Watson 1984, their Fig. 1). The fractional polarization is higher for the lower C/A , reaching 3% at $C/A = 1$ and 8% at $C/A = 0.1$ for the strong magnetic field case. When the average magnetic field is lower, the fractional polarization also is smaller (by about a factor of 2 here) as expected, indicating less anisotropy in the medium.

Another manifestation of the increase in anisotropy with stronger average magnetic fields is provided by a comparison of the representative maps of the fractional polarization at the three values $v_A/c_s = 1, 3,$ and 10 for three representative time steps in the evolution of the turbulence (Figure 3 and 4). The linear dimension of the cube is taken to be 0.12 pc , which corresponds to $N_{\text{CO}} \approx 10^{16} \text{ cm}^{-2}$ for the adopted values of $C/A \approx 0.1$ and the assumed CO abundance (10^{-4} relative to H_2). We use this column density, which is an order of magnitude higher than the density that provides the highest fractional polarization (see Figure 2), because it produces brighter lines. These lines will be more easily observable, and will still have appreciable fractional polarization.

The Figures differ in that the non-local approximation is used in Figure 3 to calculate the molecular populations at each grid point whereas the LVG approximation is used to calculate the populations in Figure 4. In the regime here where the Zeeman shift is much greater than the collision rate C_{ij} or the radiative decay rate A_E , the direction of the spectral line polarization that is generated at a grid point will tend to be either parallel or perpendicular to the magnetic field at that grid point. Whether the polarization is parallel or perpendicular is, in the absence of a strong external source of radiation, determined by the angle between the local velocity gradients and the magnetic field. Thus, the appearance of the polarization maps is defined by both the magnetic field structure and the velocity field structure. Since we know from Figure 1 that the average velocity gradients are strongest perpendicular to the magnetic field, the preferred direction for the polarization vectors should be perpendicular to the magnetic field (e.g., Goldreich & Kylafis 1981). Relative to the direction of the average magnetic field, this is exactly what is seen in our computations. Because of the turbulence, the actual magnetic fields at many grid points will be in directions that are different from the average. We might then expect that the direction of the polarization of the radiation that is

generated at these grid points will be neither parallel nor perpendicular to the direction of the average magnetic field. As a result, polarization directions might be expected in Figures 3 and 4 that are neither exactly parallel or perpendicular to the average magnetic field in the cube, which is along the horizontal axes in the Figures. That such polarization directions are not more common in these Figures is then noteworthy—especially for $v_A/c_s = 1$ where the variation in the directions of the local magnetic fields are greatest since the turbulent component of the magnetic field is strongest in comparison with the average magnetic field.

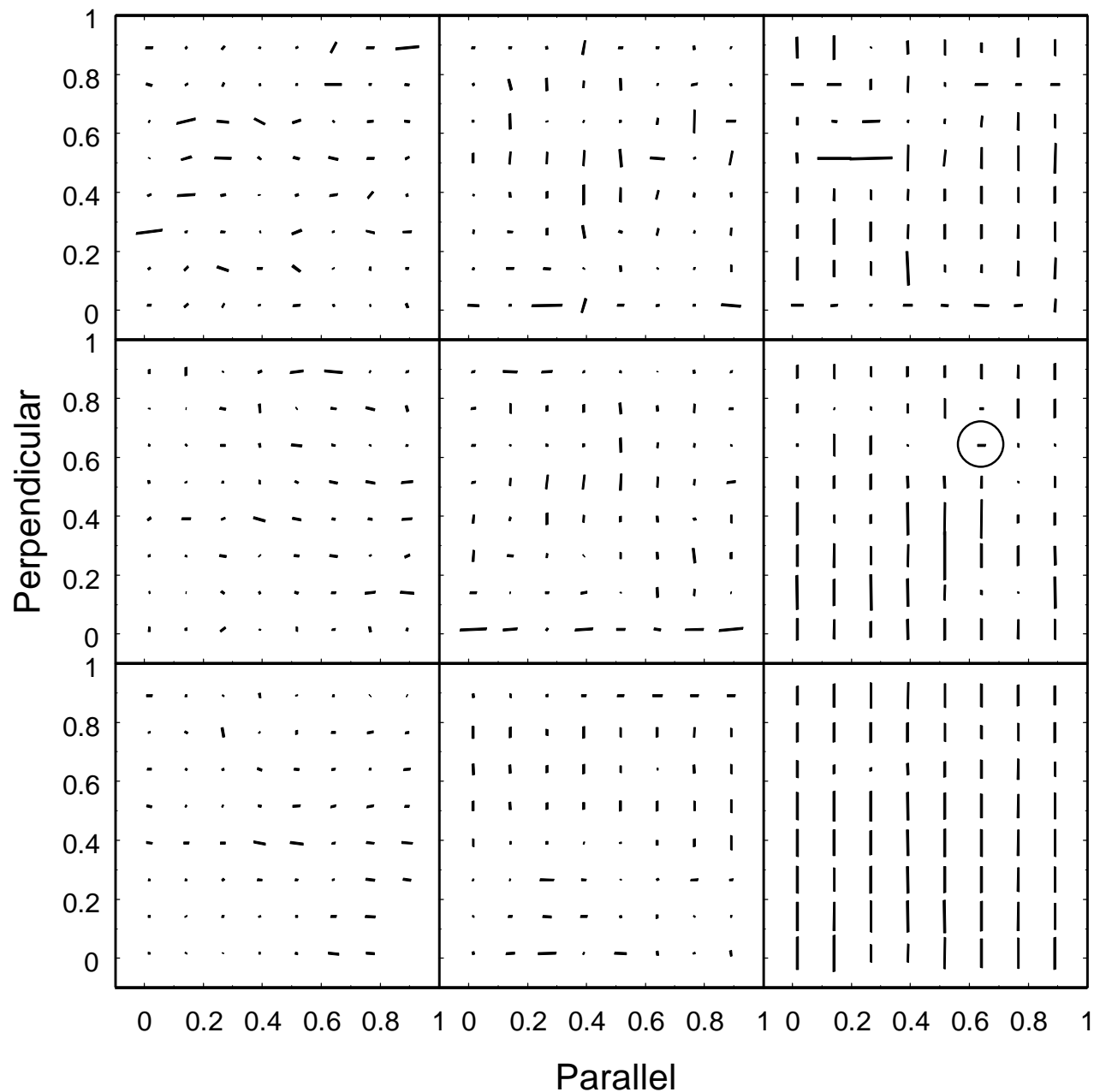


Fig. 3.— Representative maps of polarization vectors at the maximum intensity in the CO spectral line for various v_A/c_s values (1, 3, and 10 from left to right) and time steps (3rd, 5th, and 9th from top to bottom, in units of $0.2L/c_s$) obtained with the non-local approximation. The labels for the axes refer to directions parallel and perpendicular to the average magnetic field. The longest vector corresponds to the fractional polarization of 5.4%. Each 16th ray in both directions is shown. A circle marks the ray, for which line profiles are shown in Figure 5.

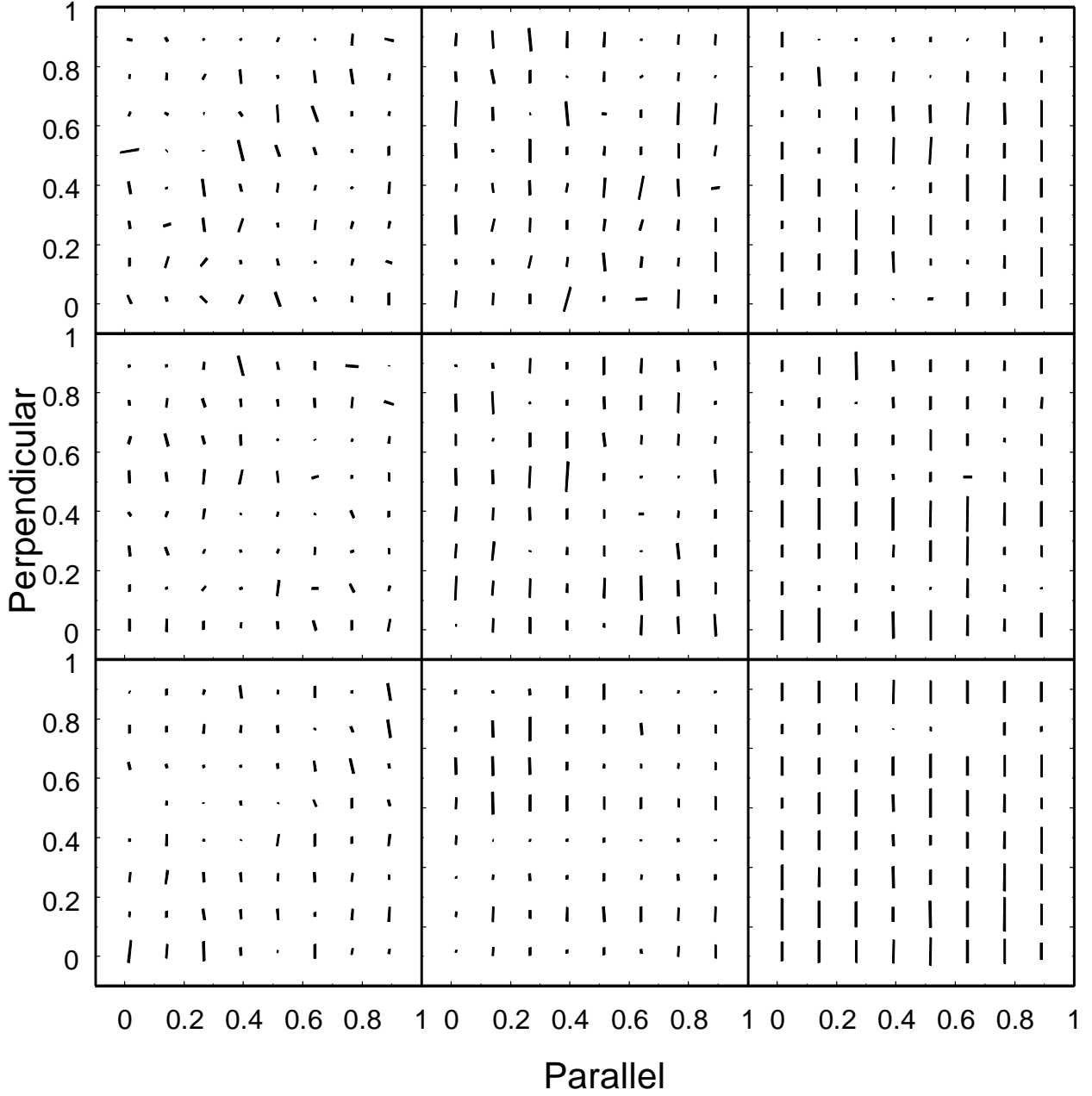


Fig. 4.— Same as in Figure 3, but obtained with the LVG approximation. The longest vector corresponds to the fractional polarization of 4.0%.

A few trends are evident in Figures 3 and 4. The fractional polarizations are greater in models with stronger magnetic fields, where we expect the anisotropy related to the MHD turbulence to be greatest. Also, the pattern of the polarization directions is more regular in the models with the stronger magnetic fields. In the $v_A/c_s = 1$ case, the polarization vectors do reflect the presence of the significant, irregular component of the magnetic field. In models with the stronger average magnetic fields (i.e., larger v_A/c_s), the only variations in the directions of the polarization that persist are at locations where the polarization directions are parallel to the average magnetic field, instead of perpendicular to it. The number of these polarization “reversals”—where the polarization direction is parallel rather than perpendicular to the average magnetic field—constitutes almost one third of the total number of rays that are considered for the non-local computations when $v_A/c_s = 3$, while only a few reversals are seen the $v_A/c_s = 10$ case. Also, in the latter case the number of reversals decreases with time. Reversals indicate that, despite the general tendency for the velocity gradients to be perpendicular to the average direction of the magnetic field, there are some locations where they are mostly parallel to the average magnetic field.

We have performed computations in which the irregularities in the magnetic fields (but not in the velocities) are artificially removed, and obtained essentially the same results. We thus conclude that the reversals are mainly due to the changes in direction of the velocity gradients.

Figures 3 and 4 do not agree well in detail on a point-by-point basis. The LVG maps are more regular, and have a smaller number of reversals. The profiles for the emergent intensities that are calculated for the LVG approximation and for the non-local approximation are somewhat different when the line is optically thin, even though they almost coincide when the column density exceeds 10^{16} cm^{-2} ($\tau \gtrsim 10$). While the Stokes-Q profiles for the two approximations are also similar at most locations, there are some points where the specific velocity structure causes the polarization vector to be parallel to the average magnetic field in the non-local case and perpendicular to it in the LVG case or vice versa. We nevertheless interpret the general agreement in the character and in the average magnitude of the polarization obtained with the two approximations as support for our working hypothesis that these approximate methods provide useful results.

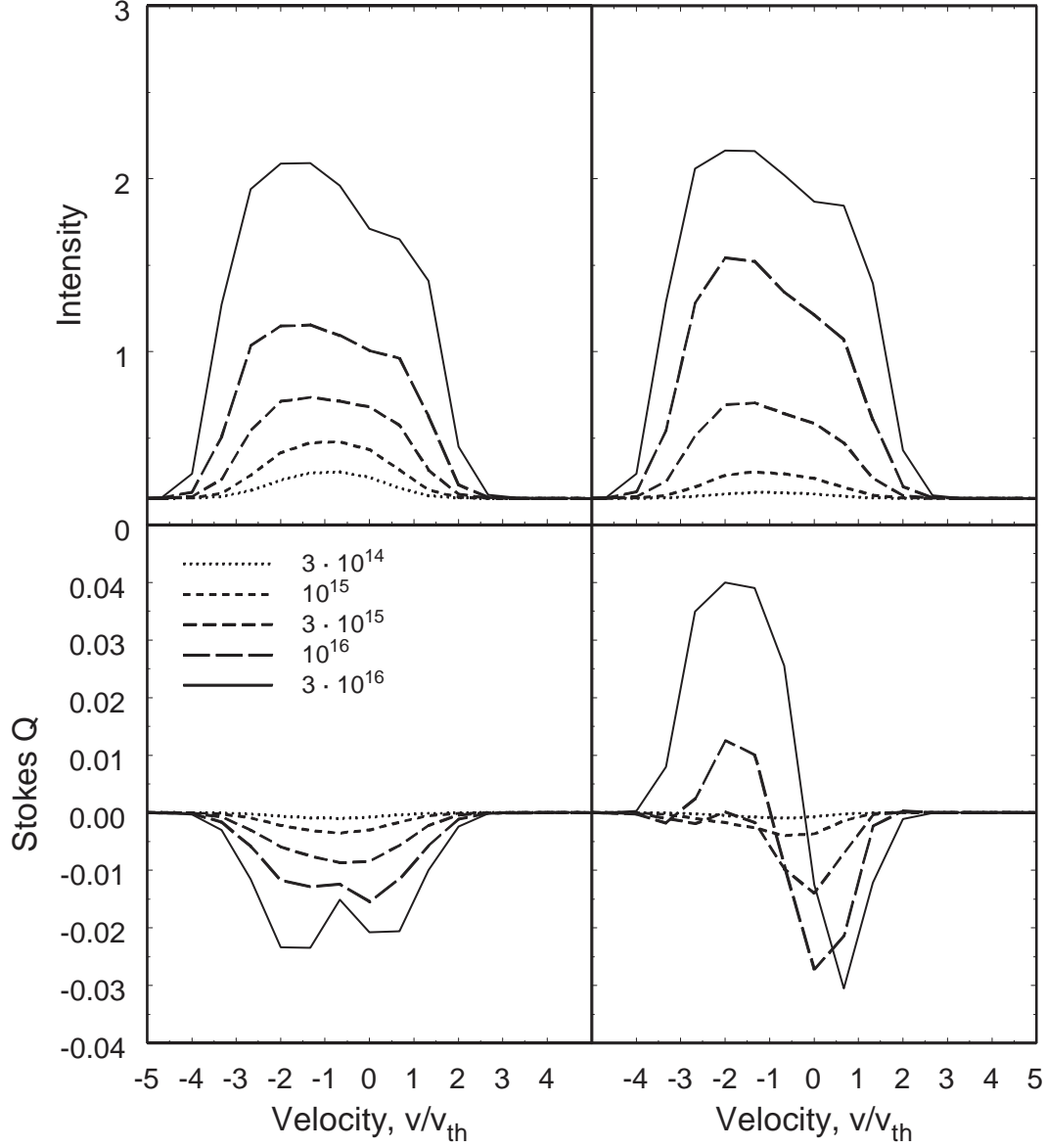


Fig. 5.— Representative intensity and Stokes-Q profiles (arbitrary intensity units) obtained with the LVG (left panels) and non-local (right panels) approximations and $v_A/c_s = 10$ (5th time step). Profiles are presented for several values of the column density N_{CO} (cm^{-2}) of CO molecules as indicated by the line types.

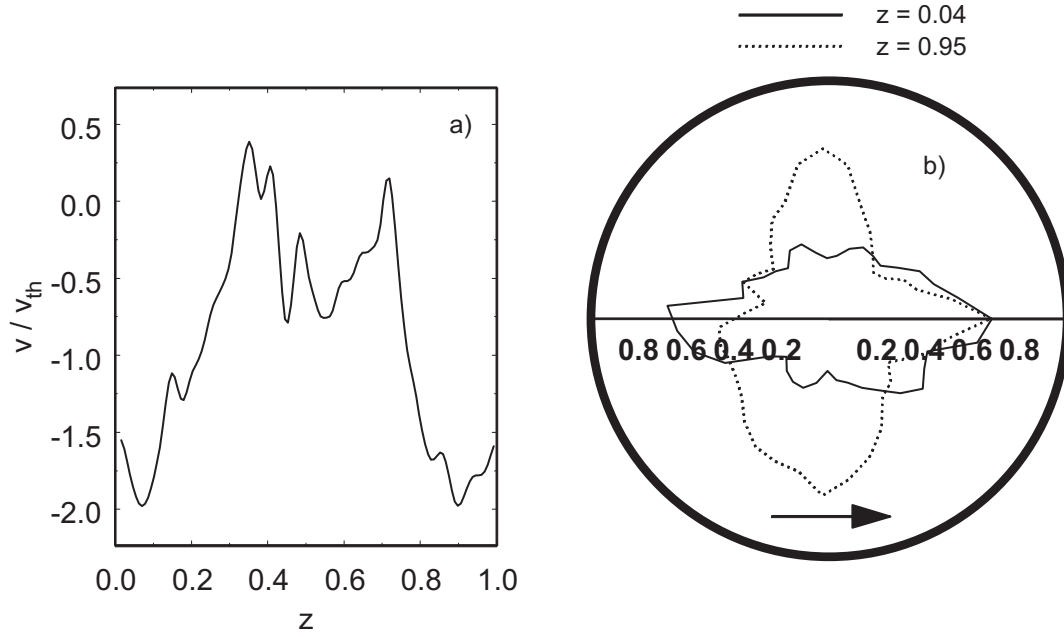


Fig. 6.— (a) The component of the turbulent velocity along the line of sight and (b) the angular distribution of the effective interaction length L_{eff} (arbitrary units) in the plane of the sky for two locations along the ray where the contributions to the polarization are orthogonal to one another. An arrow indicates the direction of the average magnetic field and z is the distance along the ray measured from the far side of the cube.

The two methods are further compared in Figure 5, where the line profiles for a single ray of radiation (the intensity that emerges from a single grid point on the surface) are given for several values of N_{CO} . The specific ray shown is the ray marked with a circle in Figure 3. This is one of the cases where the polarization vector (representing the polarization at the peak of the intensity profile) is parallel to the average magnetic field in the non-local case and perpendicular to it in the LVG case. This ray is, thus, not typical but instead represents a case where the differences between the results with the two approximate methods are greatest.

The reason for this behavior is indicated in Figure 6, where we show the variations in the LOS component of the turbulent velocity along this ray. Profiles for Stokes- I and Q of the emergent radiation are shown in Figure 5. The spectral line consists of two components with mutually perpendicular polarizations, as indicated by the sign of Q in bottom left panel (in this Paper, negative Q corresponds to polarization that is perpendicular to the direction of the average magnetic field).

Orthogonal polarizations originate in these two velocity components because of the detailed behavior of the velocity field along the ray. The component at the line-of-sight (LOS) velocities between about $-0.5v_{\text{th}}$ and $0.5v_{\text{th}}$ which occurs at distances z between $0.3L_0$ and $0.7L_0$ from the far side of the cube, has polarization perpendicular to the magnetic field. The component with LOS velocities near $-1.5v_{\text{th}}$ originates from gas at two locations along the ray, specifically, at $z < 0.3L_0$ and $z > 0.7L_0$. The region at the far side of the cube generates emission that is polarized perpendicular to the magnetic field because the effective interaction length (Eq. [2]) is largest there along the direction of the average magnetic field (solid line in Figure 6b). This is also the case in the intermediate part of the ray. Consequently, the optical depth is larger along the magnetic field. This creates the necessary conditions for overpopulation of the $m = \pm 1$ substates, resulting in stronger σ transitions and hence polarization that is perpendicular to the magnetic field.

Closer to the near surface of the cube, the structure of the velocity field changes so that the effective interaction length and the optical depth are greater in the direction perpendicular to the magnetic field (Figure 6b; dotted line). This causes overpopulation of the $m = 0$ substate, enhanced π transitions, and hence a net polarization that is parallel to the magnetic field. When the emergent radiation consists of two (or more) velocity components with different polarizations, the resultant polarization direction is determined by the stronger of the components. As the region with the “wrong” velocity structure occupies a shorter portion of the ray than does the region with the common velocity structure, it shows up as a polarization reversal only when the optical depth along the ray is sufficiently large. That is, there are no reversals if N_{CO} is smaller than some critical value (Stokes- Q is negative

for all profiles with $N_{\text{CO}} \leq 3 \times 10^{15} \text{ cm}^{-2}$ on bottom left panel of Figure 5). The number of reversals in a particular cube increases with increasing N_{CO} (at the same time, the percentage polarization decreases). In the case of the ray in Figure 6, the angular distribution of L_{eff} shown with the dotted line in Figure 6b is only created when the radiative coupling with remote locations is taken into account. It is not evident from the angular distribution of the local velocity gradients. Hence, the polarization reversal does not appear in the LVG approximation (bottom right panel of Figure 5).

4.1. Effect of the Finite Beam Size

The polarizations shown in Figures 3 and 4 are quite high. However, the vectors plotted in these maps represent single rays and do not reflect the possible effects of averaging over the finite size for the beam of a realistic telescope. Realistic averaging may cause a cancellation of the polarization vectors and a decrease in the observed polarization percentage. Such averaging may also lead to a disappearance of the reversals in polarization direction that are observed (even for the strongest magnetic fields) in Figures 3 and 4. Another concern is whether there is some substructure between the rays in Figures 3 and 4 that is being missed. We have thus computed higher resolution maps for selected, representative regions of the surfaces of the cubes.

In the upper left panel of Figure 7, we present a high resolution map for the region centered on the reversed ray that is marked with a circle in Figure 3. The map shows the polarization vectors for all 32×32 rays emerging from the region of 32×32 grid points. In lower left panel of Figure 7 we show the same map, but averaged over rays within 8×8 squares to simulate the effect of finite beam size. Because the initial perturbations include wavelengths that are a significant fraction of L_0 , the regions exhibiting reversed polarizations can occur over an appreciable fraction of the surface of the cube, even in the case of the stronger magnetic field. Their effect on the observational data will be reduced because of the finite size of the telescope beam, though the effects will tend to persist until the beam size reaches approximately $0.1L_0$. In the case of the stronger magnetic field, the regions where these reversals occur are quite localized and beam averaging will not necessarily reduce the overall polarization when the telescope beam is centered on most locations on the surface of the MHD cube.

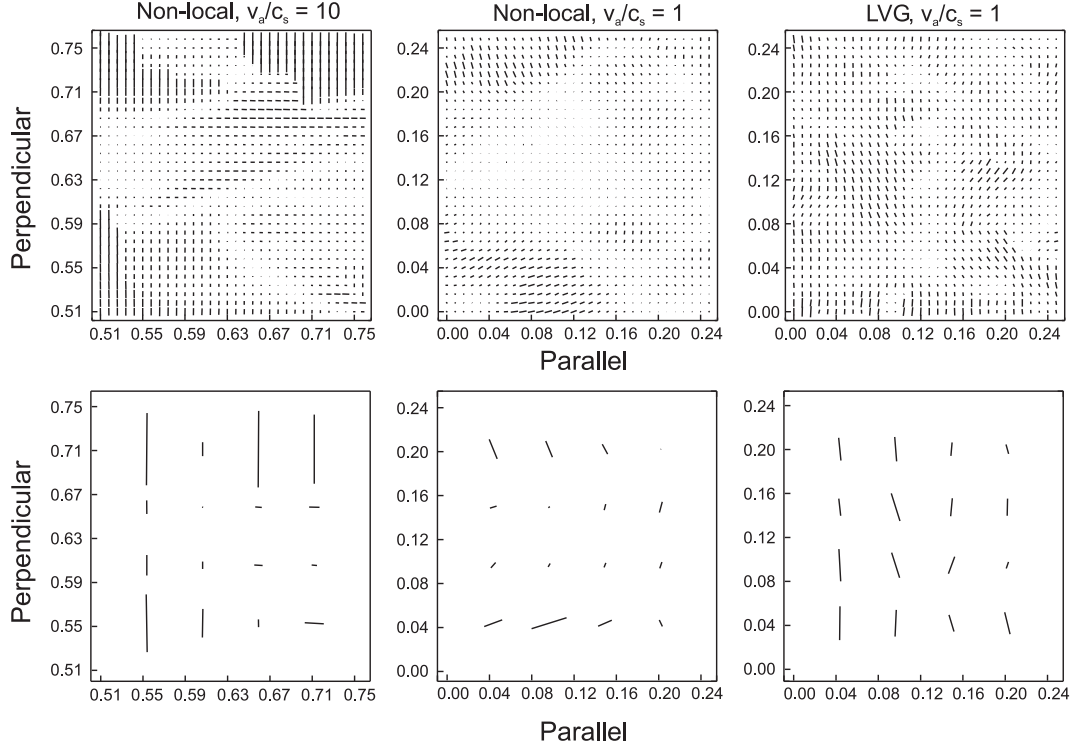


Fig. 7.— High resolution maps showing the polarization vectors for all emergent rays in 32×32 areas of grid points (top row) and with averaging over 8×8 sub-areas (lower row). Left panels—a map for a region marked with a circle on Figure 3 with $v_A/c_s = 10$. Middle panels—bottom, left corner of the surface of a cube with $v_A/c_s = 1$ obtained with the non-local approximation. Right panels—same region as in middle panels, but for the LVG approximation. The labels on the axes refer to directions parallel and perpendicular to the average magnetic field. The longest vector in the top row of maps corresponds to 2.8% and, in the lower row of maps, to 1.8% .

In the case of $v_A/c_s = 3$ where the fraction of reversed polarization vectors is about one third, mutually perpendicular polarizations within one beam are common and the resulting, observed polarization is decreased significantly by cancellation. This cancellation is even greater in the case of $v_A/c_s = 1$. In the center and right panels of Figure 7, we present high resolution maps for the lower left corner areas of the maps in Figures 3 and 4 for the $v_A/c_s = 1$ case. The vectors in the center panels of Figure 7 are computed with the non-local approximation, while the vectors in left panels are computed in the LVG approximation. Again, the maps in the lower panels are obtained by averaging the rays of the upper panels within 8×8 squares.

The polarization structure obtained in the LVG calculation is more regular, and the polarization percentage is higher, than in the non-local calculation. This difference occurs because the non-local integration encompasses a significant fraction of the cube, and the probability is high that integration paths will encounter regions with the “wrong” velocity gradients—which are plentiful in the computations with the weak magnetic fields. On a significant portion of the surface of these MHD cubes, the percentage polarization of the emerging rays is negligible. However, there are still some localized regions with the polarization at a level of 1%. The directions of the polarization vectors in these regions reflect the large-scale structure in the magnetic and velocity fields, rather than the reversed direction discussed above.

The percentage polarization is decreased by the finite beam size and averages almost to zero when the beam size is greater than $\sim 0.2L_0$. The polarization is higher in the LVG (than in the non-local) approximation and tends to be perpendicular to the average magnetic field even in the $v_A/c_s = 1$ case. Hence, the effect of the beam averaging is less dramatic in the LVG approximation.

In summary, we see that the percentage polarization is not reduced significantly for modest beam sizes in either the non-local approximation or in the LVG approximation, and persists at a level of $\sim 1\%$ even for the weakest magnetic field case that we have considered.

5. Discussion

There are now two prevailing views on the evolution of molecular clouds. According to the so called “standard” star formation scenario, molecular clouds are rather long-lived entities supported against gravity by the magnetic field (Shu et al. 1987). This support is gradually lost due to ambipolar diffusion, so that some dense clumps within a parent cloud become gravitationally unstable and collapse to form protostars. In the alternative turbulent

scenario, molecular clouds are dynamic transient objects—being formed and destroyed on a timescale which can be only slightly longer than the dynamical time (Mac Low & Klessen 2004). The existing observational data seem to favor the turbulent scenario, though the evidence can be ambiguous (Mouschovias et al. 2006).

The polarimetry of molecular lines offers further insights into the nature of chaotic motions and magnetic fields in star-forming regions as well as in other astronomical phenomena. The anisotropy of the decaying MHD turbulence has previously been shown by Watson et al. (2004) to reproduce observed polarization characteristics of OH masers. In this paper, we demonstrate that this anisotropy can also cause a linear polarization of thermal molecular lines that is similar in magnitude to what is observed. The highest fractional polarization is obtained in our calculations when the average magnetic field is strongest—where the polarization pattern also is most regular. The number of polarization reversals is greater for magnetic fields of intermediate strength, and is approximately equal to the number of polarization vectors in the “standard” direction when $v_A/c_s = 1$.

To see how this result can relate to our previous studies, we consider the polarization of the far infrared emission by dust that would result from the same magnetic field distributions. In Figure 8 we reproduce the left panel of Figure 6 from Wiebe & Watson (2004), and plot the dispersion σ_α in the position angles of the polarization vectors versus the polarization reduction factor F (which is a relative measure of the percentage polarization) using the turbulent MHD fields from the CO calculations to compute the emission by dust. In our previous studies, we were mainly interested in the relationship between the regular and irregular components of the magnetic field. Hence, we used the ratio of the strength of the random (rms) to the uniform magnetic field

$$b = B_{\text{rms}}/B_{\text{avg}} \tag{12}$$

as a main parameter. In the current study, b is a function of both time and v_A/c_s . We simulated the dust polarization in the data cubes using the same methods as in Wiebe & Watson (2004). The location of a specific point in Figure 8 depends on b and on the number of correlation lengths across the cube. The correlation length does not change significantly during the time evolution in the current simulations. Thus, the σ_α and F computed here depend only on b and lie along a single curve, denoted with the thick gray band in Figure 8. The bottom part of the band corresponds to lower v_A/c_s and/or earlier timesteps. The upper part of the band corresponds to higher v_A/c_s and/or later timesteps.

It can be seen in Figure 8 that the turbulent MHD models in our current study lead to polarization characteristics for emission by dust that overlap with the results of our computations in Wiebe & Watson (2004) only for the smallest values of v_A/c_s . On the other hand, the directions of the polarization vectors of the observed CO emission tend to be

aligned or are smoothly varying—behavior that occurs in our models for which the regular magnetic fields are stronger (values $b \lesssim 0.1$ are typical for models with $v_A/c_s \geq 3$) than those considered in our dust polarimetry project.

However, it must be stressed that thermal emission by dust and polarized CO emission trace regions that are dramatically different. The optical depth of ~ 1 that produces the highest CO polarization corresponds to $N_{\text{CO}} \approx 10^{15} \text{ cm}^{-2}$, which is equivalent to molecular hydrogen column density $N_{\text{H}_2} \sim 10^{19} - 10^{20} \text{ cm}^{-2}$ (or $A_V < 1$). This extinction is much smaller than is required to produce observable dust emission. Thus, even when the dust and the polarized CO emission are observed in the same object, the dust emission preferentially probes the inner part of the object while the polarized CO emission traces the magnetic field in the outer envelope. Our results then tend to indicate that the magnetic field is more uniform in the outer parts of such gas clouds than in the more dense core region which is responsible for the thermal emission by dust.

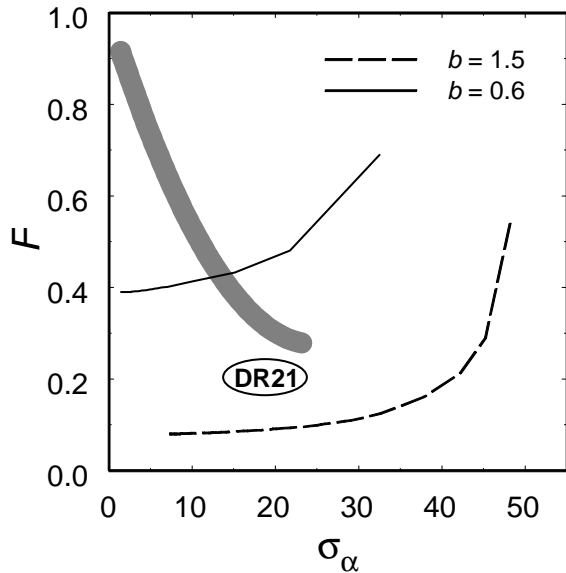


Fig. 8.— Dispersion in the position angles for the polarized emission from dust vs. polarization reduction factor for models considered in Wiebe & Watson (2004) (solid and dashed lines) and in the current paper (thick gray band). The location of a particular point on the thin lines is determined by the number of correlation lengths across the cube (increasing from right to left). The location of a point on the thick band is determined by the value of b (increasing from top to bottom). The values of σ_α and F for DR 21(OH) are computed from the observational data of Lai et al. (2003).

So far, observations provide only limited opportunities to check our predictions about the polarization of the CO lines. Unfortunately, some objects where the polarization of thermal lines has been observed are too complex to represent a case of “pure” MHD turbulence. The most appropriate is the dataset obtained for DR 21(OH). Data for the dust emission and for the CO(2–1) transition have been obtained by Lai et al. (2003), and for dust emission and the CO(1–0) transition by Cortes et al. (2005). The polarization vectors for the CO(1–0) tend to be parallel to the polarization vectors for the dust emission, whereas the polarization vectors for the CO(2–1) tend to be perpendicular to both the dust emission and the CO(1–0) vectors. Cortes et al. (2005) argued that the CO(2–1) polarization can reflect the influence of the external radiation and can then be directed parallel to the magnetic field. At the same time, the CO(1–0) polarization reflects the influence of the velocity structure and is perpendicular to the magnetic field. This is exactly the situation that is expected from our current computations. In the absence of a (strong enough) source of continuum radiation, the polarization vectors for the dust and the CO should be parallel to one another and perpendicular to the average magnetic field.

Moreover, while we have no way to relate the magnetic fields in our MHD cubes to the gravitational stability of the objects that they may represent, our results are in general agreement with the Cortes et al. (2005) conclusion that the envelope of DR 21(OH) is highly subcritical. The observation that the directions of the polarization vectors of the dust and the CO(1–0) are parallel in this object indicates that they trace the same average magnetic field and are thus correlated. However, the location of DR 21(OH) in the $\sigma_\alpha - F$ diagram (marked in Figure 8) implies the value of b is near 1. The presence of a significant irregular component as well as large scale variations in the magnetic field suggests that the field is not very dynamically important in the dense part of DR 21(OH), which is traced by the dust emission. On the other hand, the small position angle dispersion for the CO(1–0) polarization vectors corresponds to much smaller b values and, thus, to a regular magnetic field structure that is not affected by gas motions at either large or small scales.

Another detail in the observations of DR 21(OH) presented by Cortes et al. (2005) that resembles features in the current computations is the 90° change in the direction of the CO(1–0) polarization just to the West of the main polarization peak at $V_{\text{lsr}} = -10 \text{ km s}^{-1}$ (their Figure 4). However, since these “rotated” vectors are parallel to those of the CO(2–1) polarization they may just indicate the influence of a compact continuum source rather than the occurrence of the “reversals” found in this study.

Because of the low density of the gas traced by polarized CO emission, it can be used to probe the nature of the turbulence in molecular clouds more widely than just in regions of star formation. Such observations are beyond the reach of current instruments, but may be pos-

sible with ALMA—provided that ALMA has the necessary polarimetric capabilities. When these data become available, and are combined with the polarimetry data from starlight, a coherent picture of the large scale velocity and magnetic field structure in the molecular ISM may emerge.

We are grateful to Ya. Pavlyuchenkov for discussions about radiative transfer issues, and to C. Gammie and J. McKinney for continuing to allow us to use the results of their MHD computations. DW acknowledges partial support the RF President Grant NSh-4820.2006.02. Early work was also supported in part by NSF grant AST99-88104.

REFERENCES

- Barvainis, R., Wootten, A. 1987, *AJ*, 93, 168
- Cortes, P. C., Crutcher, R. M., & Watson, W. D. 2005, *ApJ*, 628, 780
- Deguchi, S., Watson, W. D. 1984, *ApJ*, 285, 126
- Deguchi, S., Watson, W. D., & Western, L. R. 1986, *ApJ*, 302, 108
- Girart, J., Crutcher, R. M., & Rao, R. 1999, *ApJ*, 525, L109
- Girart, J., Greaves, J. M., & Crutcher, R. M., Lai, S.-P. 2004, *Ap&SS*, 292, 119
- Glenn, J., Walker, Ch. K., & Jewell, P. R. 1997a, *ApJ*, 479, 325
- Glenn, J., Walker, Ch. K., Bieging, J. H., & Jewell, P. R. 1997b, *ApJ*, 487, L89
- Goldreich, P., & Kylafis, N. 1981, *ApJ*, 243, L75
- Goldreich, P. & Sridhar, S. 1995, *ApJ*, 438, 763
- Greaves, J. S., Holland, W. S., Friberg, P., & Dent, W. R. F. 1999, *ApJ*, 512, L139
- Greaves, J. S., Holland, W. S., & Ward-Thompson D. 2001, *ApJ*, 546, L53
- Greaves, J. S., Holland, W. S., & Dent, W. R. F. 2002, *ApJ*, 578, 224
- Lai, S.-P., Girart, J. M., & Crutcher, R. M. 2003, *ApJ*, 598, 392
- Lis, D. C., Goldsmith, P. F., Dickman, R. L., Predmore, C. R., Omont, A., & Cernicharo, J. 1988, *ApJ*, 328, 304

- Mac Low, M.-M., Klessen, R. S. 2004, *Rev. Mod. Phys.*, 76, 125
- Mouschovias, T. Ch., Tassis, K., & Kunz, M. W. 2006, *ApJ*, in press (astro-ph/0512043)
- Ossenkopf, V. 2002, *A&A*, 391, 295
- Shu, F. H., Adams, F.C., & Lizano, S. 1987, *ARA&A*, 25, 23
- Wannier, P. G., Scoville, N. Z., & Barvainis, R. 1983, *ApJ*, 267, 126
- Watson, W. D., Wiebe, D. S., McKinney, J. C., & Gammie, Ch. F. 2004, *ApJ*, 604, 707
- Wiebe, D. S., Watson, W. D. 2004, *ApJ*, 615, 300